ACS APPLIED MATERIALS & INTERFACES

Research Article

www.acsami.org

Highly Transparent and Durable Superhydrophobic Hybrid Nanoporous Coatings Fabricated from Polysiloxane

Ding Wang,[†,‡] Zongbo Zhang,[†,§] Yongming Li,*[,†] and Caihong Xu*[,†]

[†]Beijing National Laboratory for Molecular Sciences, Institute of Chemistry, Chinese Academy of Sciences, Beijing 100190, People's Republic of China

[‡]University of Chinese Academy of Sciences, Beijing 100049, People's Republic of China

Supporting Information

ABSTRACT: Highly transparent and durable superhydrophobic hybrid nanoporous coatings with different surface roughnesses were fabricated via a simple solidification-induced phase-separation method using a liquid polysiloxane (PSO) containing SiH and SiCH=CH_2 groups as precursors and methyl-terminated poly(dimethylsiloxane)s (PDMS) as porogens. Owing to the existence of $SiCH_n$ units, the hybrid material is intrinsically hydrophobic without modification with expensive fluorinated reagents. The roughness of the coating can be easily controlled at the nanometer scale by changing the viscosity of PDMS to achieve both superhydrophobicity and high transparency. The influence of surface roughness on the transparency and hydrophobicity of the coatings was investigated. The enhancement from hydrophobic to superhydrophobic with increasing surface roughness can be explained by the transition from the Wenzel state to the Cassie state. The optimum performance coating has an average transmittance higher than 85% in the visible-light range (400−780 nm), a water contact angle of 155°, and a slide angle lower than 1°. The coatings also exhibit good thermal and mechanical stability and durable superhydrophobicity, which paves the way for real applications of highly transparent superhydrophobic coatings.

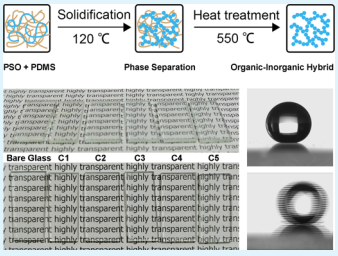

KEYWORDS: *superhydrophobicity, transparency, organic−inorganic hybrid, solidification-induced phase separation, Wenzel−Cassie transition*

1. INTRODUCTION

The term "superhydrophobic" refers to a surface with a water contact angle (CA) larger than 150° and a slide angle (SA) lower than 10°. The phenomenon that water droplets cannot adhere to such a surface but roll off the surface is advantageous for a variety of applications, for example, in protective equipment.[1−4] Transparent superhydrophobic surfaces expand the range of potential applications to optical fields such as greenhouses, safety goggles, windshields, solar cell panels, and windows for electronic devices[5−7] and therefore have recently attracted increasing attention.

Realizing the two essential properties of superhydrophobic surfaces, suitable surface roughness and low surface energy,[8,9] requires the combination of advanced design techniques and materials. The practical application of superhydrophobic surfaces relies on simple and economical fabrication approaches as well as the durability of the products. Present fabrication approaches include etching,[10−12] lithography,[13] electrochemical deposition,[14] physical/chemical vapor deposition,[15,16] electrospinning,[17,18] nano/microparticle assembly,[19−21] templating,[22,23] sol−gel process,[24,25] and phase separation.[26,27] Among these approaches, phase separation can afford polymer microstructures using relatively simple procedures that do not require corrosive reagents, special equipment, or harsh experimental conditions, which give it great potential for industrial-scale production. Up to now, superhydrophobic surfaces have been fabricated by phase separation in solvent−nonsolvent systems,[27] vapor-induced phase separation of copolymers,[28] phase separation of polymers with different solubilities,[29] polymerization-induced phase separation (PIPS) of monomers and porogens,[30] etc. The fabrication processes based on phase separation usually consist of only one or two steps without sophisticated experimental procedures. The resulting polymer surfaces have relatively low surface energies compared with inorganic materials such as silica particles. For instance, Du et al.[26] fabricated superhydrophobic poly(2-octyl cyanoacrylate) coatings with CAs of around 157° by a facile one-step method in which monomer-covered surfaces were immersed in aqueous ethanol to promote polymerization accompanied by phase separation. Erbil et al.[27] produced superhydrophobic isotactic polypropylene coatings with CAs reaching 160° by simply dropping the polymer solution onto the substrate and evaporating the solvent to induce phase separation.

Although superhydrophobicity is easily achieved, the fabrication of transparent superhydrophobic surfaces by phase separation remains a challenge. This is, in part, because the essential property of superhydrophobicity, surface roughness, is unfavorable for transparency because of light scattering. It has been demonstrated that, for the fabrication of highly trans-

Received: December 23, 2013
Accepted: February 10, 2014
Published: February 10, 2014

parent superhydrophobic surfaces, it is necessary to control the roughness below 100 nm (i.e., on a scale much smaller than the wavelength range of visible light) to effectively lower the intensity of Mie scattering.[31] Achieving such nanoscale roughness makes the fabrication process difficult. Microphase separation of polymer materials is essentially a chemical kinetic process. Adjustment of the phase-separation scale requires not only careful selection of the raw materials but also precise control over the experimental conditions, such as the type of solvent, temperature, and pressure. Some researchers have made efforts to fabricate transparent superhydrophobic surfaces with nanoscale phase separation. Levkin et al.[32] created superhydrophobic poly(butyl methacrylate-*co*-ethylene dimethacrylate) coatings through PIPS followed by soaking of the porogens in methane. Transparency was achieved by changing the composition of the polymerization mixtures, but superhydrophobicity was lost at the same time. Fluorinated acrylic material was then grafted onto the transparent surfaces to regain superhydrophobicity accompanied by a 5−10% decrease in the transmittance, which complicated the fabrication procedure and increased the production cost. Kato and Sato[30] fabricated superhydrophobic ethylene glycol dimethacrylate based polymer coatings by UV-curing-induced phase separation and subsequent ethanol flushing of the porogens. The spinning rate was tuned to control the phase-separation scale and thickness of the coating for transparency. The coating spin-coated at 7000 rpm using methyl myristate based porogen was highly transparent; however, one of the curing monomers was also a fluorinated acrylic material, and the thickness of the highly transparent coating was restricted to 250 nm. To the best of our knowledge, until now, no highly transparent superhydrophobic fluoride-free surfaces have been fabricated by the phase-separation method with controllable nanoscale phase separation. In addition, the polymeric materials widely used in the phase-separation method suffer from degradation induced by heat, oxygen, and UV irradiation, which is detrimental to long-term superhydrophobicity. Therefore, this limits the practical applications of the superhydrophobic polymer coatings under harsh conditions.

In this paper, a simple solidification-induced phase-separation method[33−38] has been adopted to fabricate highly transparent and durable superhydrophobic hybrid coatings using a liquid polysiloxane (PSO) containing SiH and SiCH═CH_2 groups as the precursor and methyl-terminated poly(dimethylsiloxane)s (PDMS) as a porogen, both of which are inexpensive and environmentally friendly. As illustrated in Figure 1, the solvent-free mixture of PSO and PDMS is spin-coated onto the substrate, followed by the catalyzed solidification of PSO, in which phase separation between PSO and PDMS takes place and the phase-separation scale is easily controlled by the viscosity of PDMS. The subsequent heat treatment transforms the solidified PSO into an organic−inorganic hybrid state, which is intrinsically hydrophobic because of the existence of $SiCH_n$ units and more stable to heat, oxygen, and UV irradiation compared with polymeric materials. PDMS is decomposed and eliminated after the heat treatment, leading to the generation of nanoporous rough surfaces. This represents the first example of the fabrication of highly transparent superhydrophobic coatings by the phase-separation method without using expensive fluorinated reagents. The PSO-derived organic−inorganic hybrid material endows the coatings with good mechanical strength, relatively high thermal stability, and, most importantly, durable superhydrophobicity.

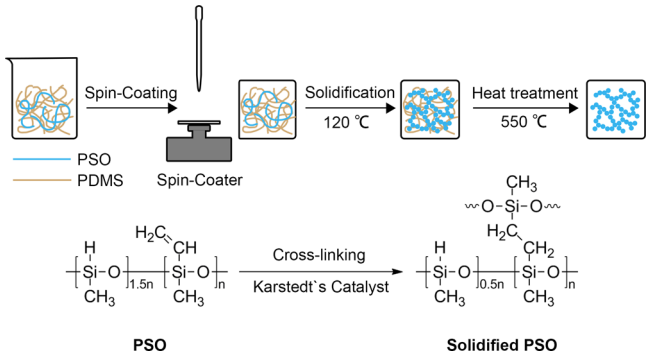

Figure 1. Schematic illustration of the fabrication procedures of the hybrid nanoporous coatings and the cross-linking formula of the platinum-catalyzed hydrosilylation reaction of the SiH and SiCH═CH_2 groups in the solidification process of PSO.

Moreover, the nanoscale surface roughness of the coating can be easily adjusted with this simple phase-separation method, and the high transparency does not rely on reducing the thickness of the coating.

2. EXPERIMENTAL SECTION

Polysiloxane (PSO) containing both SiH and SiCH═CH_2 groups was used as the precursor. Methyl-terminated poly(dimethylsiloxane)s (PDMS; Hangping Chemical Co., Beijing, China), which decompose completely under 550 °C, were used as porogens. The samples were denoted as C0, C1, C2, C3, C4, and C5 using PDMSs with different viscosities (Table 1) and fabricated as follows. First, PSO and PDMS were mixed with a weight ratio of 15:85. A total of 2 ppm (weight ratio to the mixture of PSO and PDMS) of Karstedt's catalyst (a platinum divinyltetramethyldisiloxane complex in divinyltetramethyldisiloxane; 1.5 wt % platinum; prepared by a standard procedure[39]) was subsequently added dropwise under vigorous stirring. After the addition, the mixture was continuously stirred for 30 min at room temperature. The as-prepared mixture (volume: 0.2 mL) was then spin-coated at 2000 rpm (acceleration: 2000 rpm s^{-1}) for 40 s on glass substrates and solidified in an oven at 120 °C for 6 h. Finally, the samples were heated at 550 °C for 1 h under an argon atmosphere in a Clock Hood-type furnace. The typical ramp rate was 2 °C min^{-1} at 20−250 °C and 0.5 °C min^{-1} at 250−550 °C.

The chemical composition of the organic−inorganic hybrid material was examined by Fourier transform infrared spectroscopy (FTIR; TENSOR 27, Bruker) and solid-state magic-angle-spinning (MAS) ^{29}Si and ^{13}C NMR (Avance III-400, Bruker) analyses. The microstructures of the coatings were observed by scanning electron microscopy (SEM; S-4800, Hitachi) operating at 15 kV. The microdomain sizes of the coatings were estimated by software analysis (*SMile View 2.1*, JEOL) of the SEM images. The values reported were the averages of 50 measurements of different microdomains. The pore diameters, porosities, and total pore areas of the coatings were determined by mercury pressure porosimetry (Pore Master 60GT, Quantachrome Instruments). The surface morphologies of the coatings were examined by atomic force microscopy (AFM; Nanoscope IIIa, Digital Instruments). The surface roughnesses of the coatings were estimated by software analysis (Nanoscope Analysis 1.20, Veeco) of the AFM images. The water CAs of the coatings were determined using a contact-angle goniometer (DSA 100, Krüss) at ambient temperature. The volume of the water droplets was approximately 3 μL delivered using a micropipet for static CAs and 10 μL delivered using the needle of the goniometer for SAs. The water CA and SA values reported were the averages of five measurements made on different areas of the coatings. The transmission spectra of the coatings in the range between 300 and 800 nm were recorded using a UV−vis spectrometer (U-3900, Hitachi) with a spectral resolution of 2 nm. The thermal behaviors of PDMSs with different viscosities and the organic−inorganic hybrid material were investigated

Table 1. Influence of Different PDMS Viscosities on the Physical Properties of the C0−C5 Coatings

	PDMS viscosity (cP)	microdomain size (nm)	average pore diameter (nm)	roughness (rms[a], nm)	CA (deg)	SA (deg)
C0	−[b]	−	−	2.5	97.5 ± 2.2	adhesion
C1	10	32 ± 6	23	24.4	142.2 ± 2.7	adhesion
C2	15	37 ± 5	23	27.3	152.0 ± 0.5	<1
C3	20	41 ± 1	45	30.6	155.0 ± 0.6	<1
C4	30	47 ± 2	85	50.9	155.8 ± 1.4	<1
C5	50	52 ± 2	141	87.7	155.9 ± 0.3	<1

[a]rms = root-mean-square, which gives the standard deviation of the height values. [b]−, not used or not determined.

by thermogravimetric analysis (TGA; TG/DTA6300, Seiko Instruments Inc.) with a heating rate of 10 °C min^{-1}. TGA of PDMSs were performed in argon from 50 to 800 °C, and TGA of the hybrid material was performed in air from 50 to 500 °C. The mechanical stability of C2 and C3 was evaluated by the water drop test,[19,20] in which 1500 water droplets (ca. 50 μL; impact velocity = 10 m s^{-1}; compression stress = 0.6 N) were dropped from a height of 5 m above the C2 and C3 coatings on glass substrates, respectively. The CAs, SAs, and transmission spectra of the coatings were measured after impact.

3. RESULTS AND DISCUSSION

3.1. Organic−Inorganic Hybrid Material. The organic−inorganic hybrid material was derived from the polymer precursor PSO through two fabrication processes: solidification and heat treatment. The solidification process transforms PSO from a liquid linear polymer into a three-dimensional cross-linked network. The solidified PSO then forms an organic−inorganic hybrid material upon subsequent heat treatment at 550 °C. The FTIR spectra of PSO, solidified PSO, and the hybrid coating C0 are shown in Figure 2. In the FTIR curve of

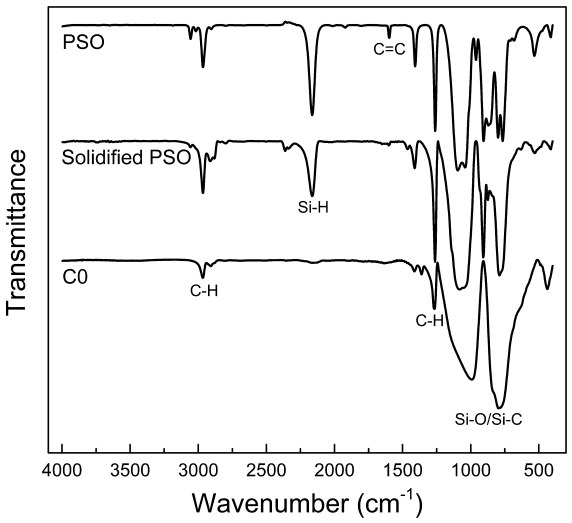

Figure 2. FTIR spectra of PSO, solidified PSO, and C0.

PSO, the absorption peaks at 2164 and 1599 cm^{-1} are the characteristic absorptions of the SiH and SiCH=CH_2 groups, respectively. According to the cross-linking formula in Figure 1, the platinum-catalyzed hydrosilylation reaction in the solidification process consumes equal amounts of SiH and SiCH=CH_2 groups, and the molar ratio of the two groups in PSO is 1.5:1; therefore, the SiH groups in PSO are in excess. As a result, there is a weaker absorption peak of SiH groups in the FTIR spectrum of solidified PSO (Figure 2). The remaining SiH groups undergo SiH/SiO redistribution reactions at higher temperatures, forming T ($CSiO_3$) units and releasing gas according to the following equations:[40,41]

$$3D^H \rightarrow MeSiH_3 + 2T \quad (1)$$

$$4D^H \rightarrow (MeH_2Si)_2O + 2T \quad (2)$$

where D^H = $CSi(H)O_2$ and T = $CSiO_3$. Consequently, there is almost no absorption peak of SiH groups in the FTIR spectrum of C0. During the polymer−ceramic transformation (i.e., the organic−inorganic transformation of PSO), the cleavage of C−H bonds usually starts at 600 °C.[42] The peaks in the 2850−3000 cm^{-1} range and at 1265 cm^{-1} for C0 relate to the vibration of C−H in $SiCH_n$ groups, indicating that the C−H bonds persist through heat treatment at 550 °C. The peaks in the 700−1250 cm^{-1} range of all curves are ascribed to the vibrations of the Si−O and Si−C bonds. The sharp and sophisticated peaks in PSO become two broad peaks in C0, signifying relatively ordered Si−O−Si and Si−C−Si networks in the organic−inorganic hybrid material.

Figure 3a shows the MAS ^{29}Si NMR spectra of solidified PSO and C0. The two main resonances in solidified PSO centered at −19 and −33 ppm can be assigned to D (C_2SiO_2) units, generated by the cross-linking of SiH and SiCH=CH_2 groups (Figure 1), and D^H ($C(H)SiO_2$) units, representing the excess SiH groups, respectively. After heat treatment at 550 °C, the resonance of the D^H units disappears, indicating the consumption of excess SiH groups, which is in accordance with the FTIR results. Additionally, two new resonances appear in the C0 spectrum centered at 6 and −65 ppm, which can be assigned to M (C_3SiO) and T ($CSiO_3$) units, respectively. The T units confirm the aforementioned SiH/SiO redistribution reactions (eqs 1 and 2), and the M units provide evidence for the SiO/SiC redistribution reactions, which are the critical reactions in the high-temperature ceramization process of PSO.[37] The equations are

$$2D \rightarrow M + T \quad (3)$$

$$D + T \rightarrow M + Q \quad (4)$$

$$D + M \rightarrow C + T \quad (5)$$

$$D + Q \rightarrow 2T \quad (6)$$

where C = SiC_4, M = C_3SiO, D = C_2SiO_2, T = $CSiO_3$, and Q = SiO_4. The equilibrium of these reactions depends on the materials used and the processing temperature. It is shown in Figure 3a that the resonances of the M, D, and T units are dominant in C0, which is an intermediate state between polymer and ceramic.[43] Solidified PSO becomes an organic−inorganic hybrid material through these redistribution reactions (eqs 1−6), which can further cross-link and strengthen the Si−O−Si and Si−C−Si networks, leading to a relatively rigid structure of the final coatings. The MAS ^{13}C NMR spectrum of

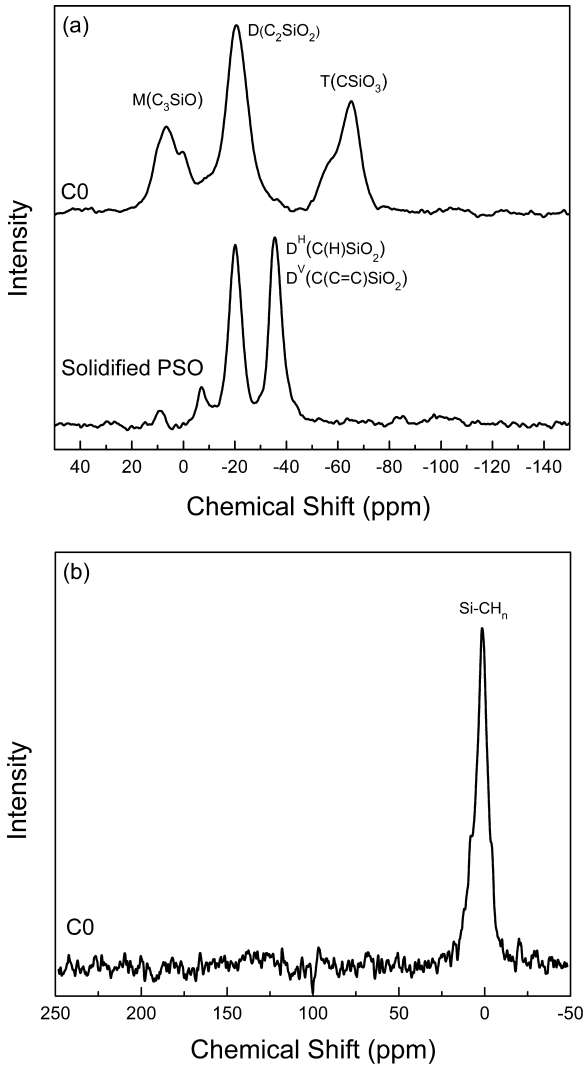

Figure 3. (a) MAS ^{29}Si NMR spectra of solidified PSO and C0. (b) MAS ^{13}C NMR spectrum of C0.

C0 is shown in Figure 3b. The resonance centered at 1.5 ppm is attributed to the carbon in the $SiCH_n$ units, in agreement with the FTIR spectrum of C0. The FTIR and NMR results above verify that the organic−inorganic hybrid material contains Si−O, Si−C, and C−H bonds. The possible structure of the hybrid material is presented in Figure 4. The hydrophobic C−H bonds are the main reason for the intrinsic hydrophobicity of the hybrid material, which has a CA of 97.5° at the smooth C0 surface.

3.2. Microstructure and Surface Morphology. The SEM images of the hybrid coatings prepared using PDMSs with different viscosities (Table 1) are shown in Figure 5, together with that of C0 (fabricated without PDMS) for comparison. It can be observed from Figure 5 that C0 is very smooth and that all of the other coatings have similar microstructures consisting of interconnected microdomains and nanopores. The development of nanoporous microstructures is due to phase separation between PSO and PDMS. On the basis of the similarity of the PSO and PDMS molecules (i.e., they both have Si−O−Si skeletons with $SiCH_3$ groups), they are compatible with each other in the mixture. During the solidification process of PSO, the cross-linking reaction of SiH and $SiCH{=}CH_2$ groups gradually transforms PSO through diffusion from a homogeneously dispersed linear polymer into interconnected solid microdomains. The porogen PDMS with higher viscosity directly lowers the diffusion rate of the catalyst and PSO molecules and thereby reduces the cross-linking reaction rate of PSO, leading to greater phase separation. PDMS is then decomposed and eliminated by the heat treatment at 550 °C (Figure S1 in the Supporting Information, SI), accompanied by a shrinkage of about 5% of the thickness of the coating. Owing to the microdomains and nanopores between them, the surfaces of the coatings become rough, which can be seen from the AFM images in Figure 6. The nanoscale phase separation can be easily adjusted by changing the viscosity of PDMS, resulting in tunable surface roughness of the coating.

The microdomain sizes estimated from the SEM images and the average pore diameters determined by mercury pressure porosimetry are listed in Table 1. (The microdomain size and pore diameter distributions are shown in Figures S2 and S3 in the SI.) The porosities and total pore areas determined by mercury pressure porosimetry are listed in Table S1 in the SI to

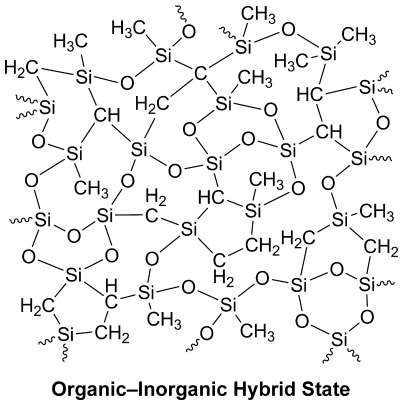

Figure 4. Possible structure of the organic−inorganic hybrid material.

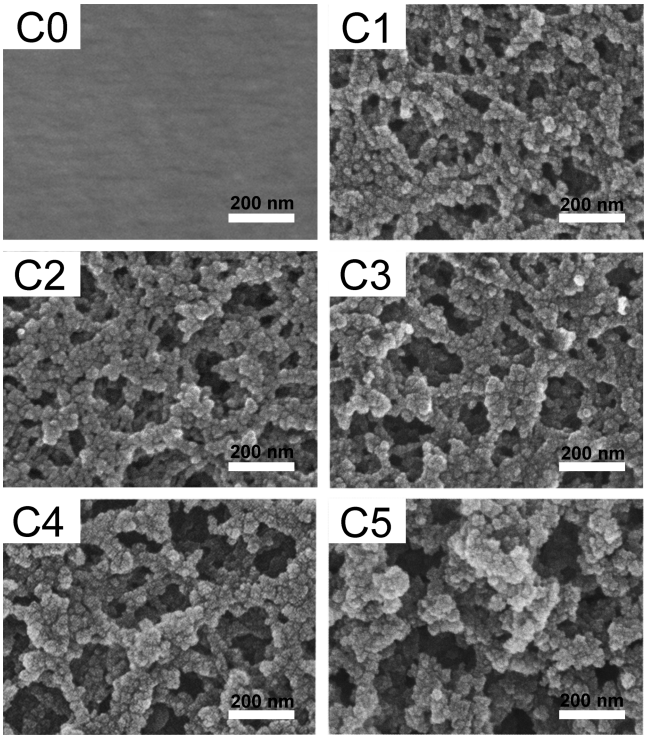

Figure 5. SEM images of the C0−C5 coatings.

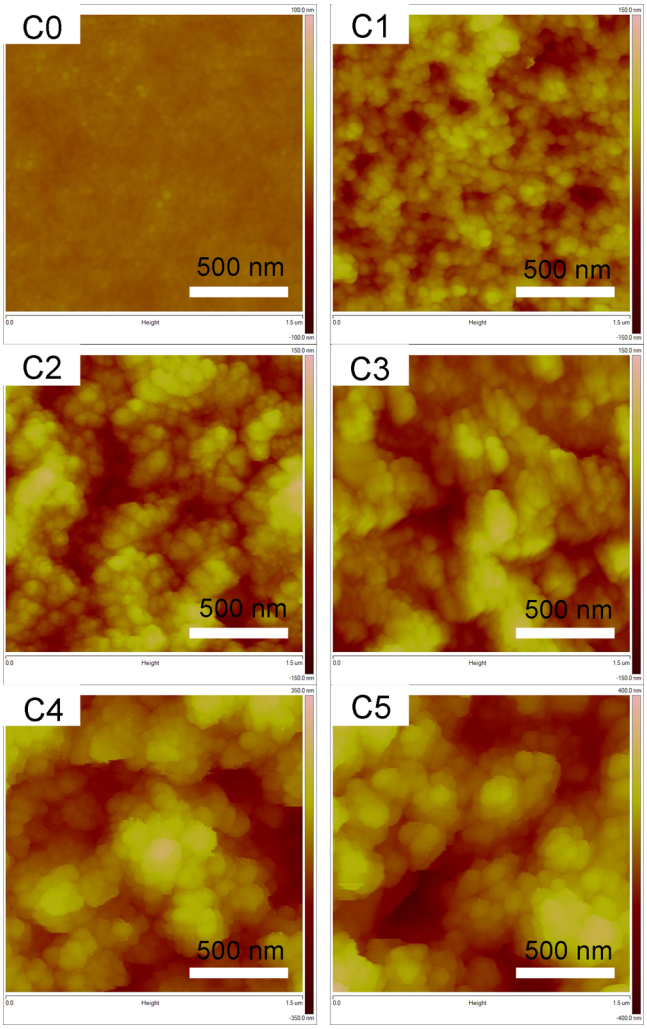

Figure 6. AFM images of the C0−C5 coatings.

give more information concerning the nanoporous structure. The results in Table 1 confirm the influence of the viscosity of PDMS on the scale of phase separation. With increasing viscosity of PDMS from 10 to 50 cP, the microdomain size increases from 32 to 52 nm and the average pore diameter increases from 23 to 141 nm, corresponding to an increasing larger scale of phase separation from C1 to C5. Accordingly, the total pore area of the coating decreases from 287.9 to 104.5 $m^2 g^{-1}$ based on similar porosities around 83% (Table S1 in the SI). The root-mean-square (rms) roughness values, which represent the standard deviation of the roughness from the height obtained from software analysis of the AFM images, are also listed in Table 1. This shows that C0 has a small rms roughness of 2.5 nm, which reflects a smooth surface. The rms roughness increases from 24.4 to 87.7 nm for C1−C5, which is the same variation tendency as the scale of phase separation. It is noted that the rms roughnesses are all below 100 nm. Such small values are sufficient to reduce the scattering of visible light, which is the reason for the high transparency of the coatings.

3.3. Hydrophobicity. The water CAs and SAs of C0−C5 were investigated to examine the hydrophobicity of the coatings. The results are shown in Table 1 and Figure 7. The intrinsic CA of the smooth coating C0 is 97.5°, which is hydrophobic because of the composition of the hybrid material,

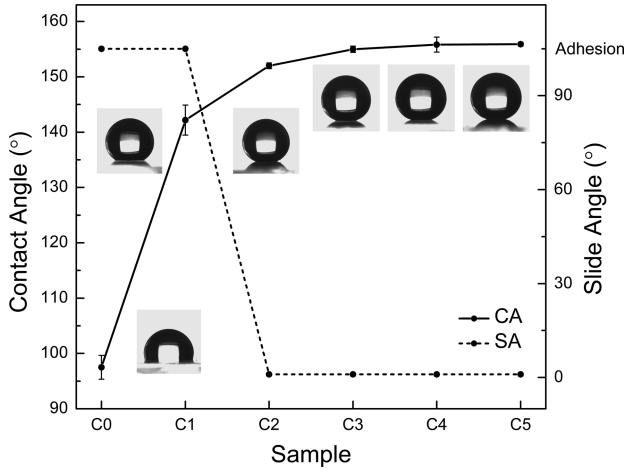

Figure 7. Water CAs and SAs of the C0−C5 coatings.

as demonstrated above. With increasing surface roughness from C1 to C5, the CA increases initially from 142.2° to 155.0° and then remains almost constant around 155°. The water droplets on C0 and C1 never roll off even when the glass slide is turned upside-down. The SAs of C2−C5 are all identified as less than 1° because the deposited water droplets slide off immediately after they are separated from the needle when the glass slide is tilted at an angle of 1° (video S1 in the SI). On the basis of these results, C2−C5 are identified as superhydrophobic coatings.

The enhancement from hydrophobic to superhydrophobic with increasing surface roughness of the coatings can be explained by the transition from the Wenzel state to the Cassie state.[44] According to the Wenzel model (eq I),[45] the air entrapped in the voids of the substrate can be excluded by water droplets and a solid/liquid interface can form. The apparent Wenzel CA, θ^W, is defined as

$$\cos \theta^W = r \cos \theta_0 \quad \text{(I)}$$

where r is the roughness factor and is defined as the ratio of the true surface area to the horizontal projection of the surface area (r is larger than unity) and θ^0 is Young's CA determined on a smooth surface of the same nature. Equation I predicts an increase of θ^W with increasing r when the substrate is intrinsically hydrophobic ($\theta^0 > 90°$). In contrast, in the Cassie model (eq II),[46] water droplets are suspended beyond the air entrapped in the voids of the substrate and a solid/liquid/air composite interface forms. The apparent Cassie CA, θ^C, is defined as

$$\cos \theta^C = f(\cos \theta_0 + 1) - 1 \quad \text{(II)}$$

where f is the fraction of solid/liquid contact. Equation II predicts an increase of θ^C with decreasing solid/liquid contact in which increasingly more air is entrapped in the voids. In short, increasing surface roughness leads to increasing CA on Wenzel surfaces, but the surface roughness does not directly relate to the CA on Cassie surfaces. In addition, because of the decreased solid/liquid contact in the Cassie state, water droplets roll more easily on Cassie surfaces than on Wenzel surfaces, resulting in lower SAs.[47−49] It is obvious from Figure 7 that the transition from the Wenzel state to the Cassie state takes place between C1 and C2.

C0 and C1 are both in the Wenzel state. The higher surface roughness of C1 results in a higher CA of 142°. The adhesion

of water droplets on C0 and C1 is due to the tight solid/liquid contact such that the adsorption force at the interface is higher than the gravitation force acting on the droplet when the glass slide is vertical. The superhydrophobic coatings C2−C5 are in the Cassie state. The fraction of solid/liquid contact in a solid/liquid/air composite interface is determined by many parameters of the surface morphology such as the shape, size, height, and distribution of the microdomains.[13,50] Therefore, the CA no longer increases with increasing rms roughness. According to eq II, the almost constant CA of 155° for C2−C5 implies a similar fraction of solid/liquid contact (ca. 10%), resulting in extremely low SAs because the water droplets almost float upon the air pockets within the rough surfaces.

3.4. Transparency. Figure 8a shows the UV−vis transmission spectra of bare glass and the C0−C5 coatings on glass substrates. The transmittance decreases with increasing surface roughness from C0 to C5. However, the coatings are all transparent in the visible-light-wavelength range (400−780 nm), which is reflected in the easy readability of the letters underneath the coated glass slides even in the angled photograph (Figure 8b). Among the superhydrophobic coatings C2−C5, C2 has the highest average transmittance of 88.6%, very close to the value of bare glass (91.0%), in the visible-light-wavelength range. The C3 coating has a high CA of 155° and an average transmittance of 85.1%. It can be observed from the inset of Figure 8a that C0 has a slightly higher transmittance in the near-IR-wavelength range, suggesting that the refractive index of the hybrid material is between that of air and glass, which could reduce reflection at the air/substrate interface and increase transparency. However, the main reason for the high transparency of the coatings is that the surface roughness of all surfaces is less than 100 nm, far from the minimum wavelength of visible light of 400 nm. Such nanoscale roughness could reduce the particle-size-dependent Mie scattering, resulting in higher transparency with lower surface roughness. In addition, as another parameter that affects transparency, the thickness of the coatings in this work is between 2 and 7 μm (Figure S4 in the SI). In other words, the high transparency of the coatings does not rely on the thinness.

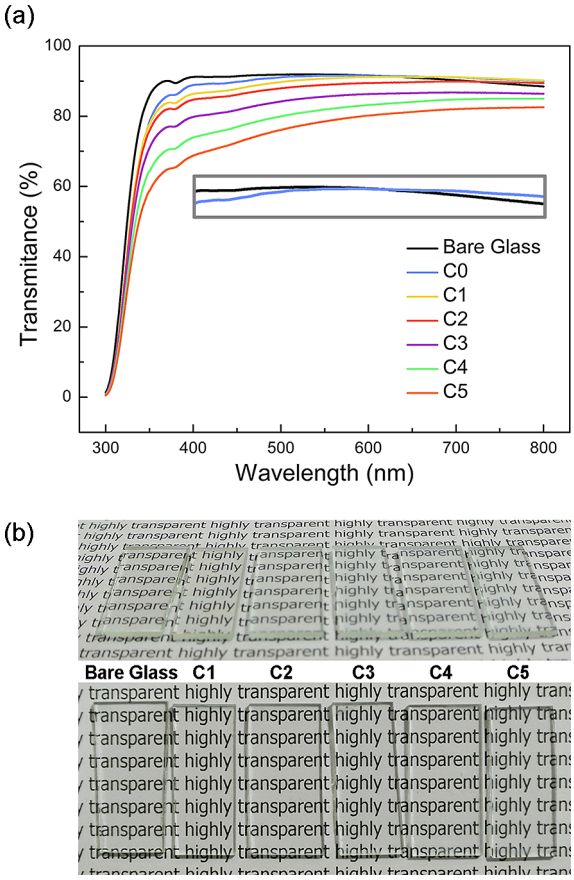

Figure 8. (a) UV−vis transmission spectra of bare glass and the C0−C5 coatings. The inset shows the magnified curves of bare glass and C0. (b) Angled (upper) and front (lower) photographs of bare glass and the C1−C5 coatings.

3.5. Thermal and Mechanical Stability and Durable Superhydrophobicity. The organic−inorganic hybrid material is relatively more stable toward heat and oxygen compared with polymeric materials. There is no weight loss in the TGA curve of the hybrid material (Figure S5 in the SI) up to 300 °C in air. The CA and SA of C3 remain unchanged after heat treatment at 400 °C for 1 h in air at 155.0° and less than 1°, respectively. The good stability toward heat and oxygen makes this material applicable in high-temperature processes where polymeric materials might melt. One of the problems for the practical application of superhydrophobic surfaces is that the elaborately designed microstructures of the rough surfaces are easily damaged because of their weak mechanical strength. However, the nanoporous structure extends through the entire thickness of the coating (Figure S4 in the SI); therefore, the surface of the coating remains nanoporous and superhydrophobic even if the top layer of the coating has been scraped off. Besides, the bonding of the coatings with the glass substrate is good, because peeling off adhesive tapes (3M Scotch Cellophane Film Tape 610, pressed with approximately 10 kPa to the coatings) does not remove the coating on the area underneath. The mechanical stability of C2 and C3 on glass substrates was examined by the water drop test, in which about 1500 water droplets (ca. 50 μL; impacting velocity = 10 m s^{-1}; compression stress = 0.6 N) are dropped from a height of 5 m above the coating. The CAs, SAs, and average transmittances in the visible-light-wavelength range of the coatings before and after impact are listed in Table 2. (The transmission spectra are shown in Figure S6 in the SI.) The superhydrophobicity and transparency of water-rinsed coatings remained almost unchanged, reflecting their good mechanical strength.

Table 2. Comparison of the Superhydrophobicity and Transparency of the Coatings C2 and C3 before and after the Water Drop Test

	CA (deg)	SA (deg)	average transmittance[a] (%)
C2	152.0 ± 0.5	<1	88.6
C2 after impact	152.3 ± 0.6	<1	88.8
C3	155.0 ± 0.6	<1	85.1
C3 after impact	155.1 ± 0.2	<1	85.0

[a]In the visible-light-wavelength range: 400−780 nm.

Another important requirement for real applications is the durability of superhydrophobicity. The CA and SA of the C3 were measured every 2 weeks after storage under ambient conditions beside the window. The superhydrophobicity of the coating remained excellent, with no change of CA and SA for 5 months. The durable superhydrophobicity results from the chemical composition of the organic−inorganic hybrid material

(Figure 4). This material has almost no active sites that form hydrogen bonds or hydrogen-bonding active groups that can undergo hydration.[51]

4. CONCLUSIONS

A simple and inexpensive solidification-induced phase-separation method has been applied to fabricate highly transparent and durable superhydrophobic (CA = 155°; SA = <1°) organic−inorganic hybrid nanoporous coatings using a liquid PSO as the precursor and PDMSs as porogens. This is the first time that highly transparent and superhydrophobic coatings have been fabricated by the phase-separation method without using expensive fluorinated reagents. The method can easily provide nanoscale surface roughness using an intrinsically hydrophobic hybrid material to fulfill the requirements of both high transparency and superhydrophobicity. The influence of the surface roughness on the transparency and hydrophobicity of the coatings was investigated. The coating changed from the Wenzel state to the Cassie state and from hydrophobicity to superhydrophobicity with increasing surface roughness. The transparency of the coating decreased with increasing surface roughness; however, the coatings were all transparent mainly because the surface roughnesses were below 100 nm. It must be emphasized that the PSO-derived organic−inorganic hybrid material endowed the coatings with good stability toward heat and oxygen and that the excellent superhydrophobicity lasted for more than 5 months. The shortcoming of the current method is the relatively high temperature for heat treatment. Further studies on the selection of porogens with lower decomposition temperature are ongoing in our laboratory. The simple and economical fabrication process, high transparency, durable hydrophobicity, and good thermal and mechanical stability of the coatings highlight their potential in practical applications such as safety goggles, windshields, solar cell panels, and windows for electronic devices.

■ ASSOCIATED CONTENT

Ⓢ Supporting Information

Video of water droplets rolling off the superhydrophobic surface of C3, TGA curves of PDMSs with different viscosities in argon with a heating rate of 10 °C min^{-1} from 50 to 800 °C, microdomain size distributions, pore diameter distributions, porosities, and total pore areas of the coatings C1−C5, SEM images of cross sections of the coatings C1−C5, TGA curve of the hybrid material in air with a heating rate of 10 °C min^{-1} from 50 to 500 °C, and UV−vis transmission spectra of C2 and C3 after the water drop test. This material is available free of charge via the Internet at http://pubs.acs.org.

■ AUTHOR INFORMATION

Corresponding Authors

*Tel.: +86-10-62554487. Fax: +86-10-62554487. E-mail: lym018@iccas.ac.cn.

*Tel.: +86-10-62554487. Fax: +86-10-62554487. E-mail: caihong@iccas.ac.cn.

Author Contributions

§Authors D.W. and Z.Z. contributed equally.

Notes

The authors declare no competing financial interest.

■ ACKNOWLEDGMENTS

The authors acknowledge financial support from the National Natural Science Foundation of China (Gran 51273205) and the Ministry of Science and Technology of China (Grants 2010CB934705 and 2012CB933200).

■ REFERENCES

(1) Kako, T.; Nakajima, A.; Irie, H.; Kato, Z.; Uematsu, K.; Watanabe, T.; Hashimoto, K. Adhesion and Sliding of Wet Snow on a Super-Hydrophobic Surface with Hydrophilic Channels. *J. Mater. Sci* **2004**, *39*, 547−555.

(2) Zielecka, M.; Bujnowska, E. Silicone-Containing Polymer Matrices as Protective Coatings: Properties and Applications. *Prog. Org. Coat.* **2006**, *55*, 160−167.

(3) Mahltig, B.; Böttcher, H. Modified Silica Sol Coatings for Water-Repellent Textiles. *J. Sol−Gel Sci. Technol.* **2003**, *27*, 43−52.

(4) Zhang, H.; Lamb, R.; Lewis, J. Engineering Nanoscale Roughness on Hydrophobic Surface—Preliminary Assessment of Fouling Behaviour. *Sci. Technol. Adv. Mater.* **2005**, *6*, 236−239.

(5) Choi, S. J.; Huh, S. Y. Direct Structuring of a Biomimetic Anti-Reflective, Self-Cleaning Surface for Light Harvesting in Organic Solar Cells. *Macromol. Rapid Commun.* **2010**, *31*, 539−544.

(6) Tadanaga, K.; Katata, N.; Minami, T. Super-Water-Repellent Al_2O_3 Coating Films with High Transparency. *J. Am. Ceram. Soc.* **1997**, *80*, 1040−1042.

(7) Lee, S. G.; Lee, D. Y.; Lim, H. S.; Lee, D. H.; Lee, S.; Cho, K. Switchable Transparency and Wetting of Elastomeric Smart Windows. *Adv. Mater.* **2010**, *22*, 5013−5017.

(8) Sun, T.; Feng, L.; Gao, X.; Jiang, L. Bioinspired Surfaces with Special Wettability. *Acc. Chem. Res.* **2005**, *38*, 644−652.

(9) Zhang, X.; Shi, F.; Niu, J.; Jiang, Y.; Wang, Z. Superhydrophobic Surfaces: From Structural Control to Functional Application. *J. Mater. Chem.* **2008**, *18*, 621−633.

(10) Song, X.; Zhai, J.; Wang, Y.; Jiang, L. Fabrication of Superhydrophobic Surfaces by Self-Assembly and Their Water-Adhesion Properties. *J. Phys. Chem. B* **2005**, *109*, 4048−4052.

(11) Qian, B.; Shen, Z. Fabrication of Superhydrophobic Surfaces by Dislocation-Selective Chemical Etching on Aluminum, Copper, and Zinc Substrates. *Langmuir* **2005**, *21*, 9007−9009.

(12) Her, E. K.; Ko, T. J.; Shin, B.; Roh, H.; Dai, W.; Seong, W. K.; Kim, H. Y.; Lee, K. R.; Oh, K. H.; Moon, M. W. Superhydrophobic Transparent Surface of Nanostructured Poly(Methyl Methacrylate) Enhanced by a Hydrolysis Reaction. *Plasma Processes Polym.* **2013**, *10*, 481−488.

(13) Öner, D.; McCarthy, T., Jr. Ultrahydrophobic Surfaces. Effects of Topography Length Scales on Wettability. *Langmuir* **2000**, *16*, 7777−7782.

(14) Shirtcliffe, N. J.; McHale, G.; Newton, M. I.; Chabrol, G.; Perry, C. C. Dual-Scale Roughness Produces Unusually Water-Repellent Surfaces. *Adv. Mater.* **2004**, *16*, 1929−1932.

(15) Tavana, H.; Amirfazli, A.; Neumann, A. W. Fabrication of Superhydrophobic Surfaces of *n*-Hexatriacontane. *Langmuir* **2006**, *22*, 5556−5559.

(16) Lau, K. K. S.; Bico, J.; Teo, K. B. K.; Chhowalla, M.; Amaratunga, G. A. J.; Milne, W. I.; McKinley, G. H.; Gleason, K. K. Superhydrophobic Carbon Nanotube Forests. *Nano Lett.* **2003**, *3*, 1701−1705.

(17) Park, S. H.; Lee, S. M.; Lim, H. S.; Han, J. T.; Lee, D. R.; Shin, H. S.; Jeong, Y.; Kim, J.; Cho, J. H. Robust Superhydrophobic Mats Based on Electrospun Crystalline Nanofibers Combined with a Silane Precursor. *ACS Appl. Mater. Interfaces* **2010**, *2*, 658−662.

(18) Ma, M.; Hill, R. M.; Lowery, J. L.; Fridrikh, S. V.; Rutledge, G. C. Electrospun Poly(styrene-*block*-dimethylsiloxane) Block Copolymer Fibers Exhibiting Superhydrophobicity. *Langmuir* **2005**, *21*, 5549−5554.

(19) Gao, L.; He, J. Surface Hydrophobic Co-Modification of Hollow Silica Nanoparticles toward Large-Area Transparent Superhydrophobic Coatings. *J. Colloid Interface Sci.* **2013**, *396*, 152−159.

(20) Xu, L.; Karunakaran, R. G.; Guo, J.; Yang, S. Transparent, Superhydrophobic Surfaces from One-Step Spin Coating of Hydrophobic Nanoparticles. *ACS Appl. Mater. Interfaces* **2012**, *4*, 1118−1125.
(21) Du, X.; Li, X.; He, J. Facile Fabrication of Hierarchically Structured Silica Coatings from Hierarchically Mesoporous Silica Nanoparticles and Their Excellent Superhydrophilicity and Superhydrophobicity. *ACS Appl. Mater. Interfaces* **2010**, *2*, 2365−2372.
(22) Xu, Q. F.; Liu, Y.; Lin, F. J.; Mondal, B.; Lyons, A. M. Superhydrophobic TiO_2−Polymer Nanocomposite Surface with UV-Induced Reversible Wettability and Self-Cleaning Properties. *ACS Appl. Mater. Interfaces* **2013**, *5*, 8915−8924.
(23) Deng, X.; Mammen, L.; Butt, H. J.; Vollmer, D. Candle Soot as a Template for a Transparent Robust Superamphiphobic Coating. *Science* **2012**, *335*, 67−70.
(24) Shang, H. M.; Wang, Y.; Limmer, S. J.; Chou, T. P.; Takahashi, K.; Cao, G. Z. Optically Transparent Superhydrophobic Silica-Based Films. *Thin Solid Films* **2005**, *472*, 37−43.
(25) Tadanaga, K.; Kitamuro, K.; Matsuda, A.; Minami, T. Formation of Superhydrophobic Alumina Coating Films with High Transparency on Polymer Substrates by the Sol−Gel Method. *J. Sol−Gel Sci. Technol.* **2003**, *26*, 705−708.
(26) Du, X.; Li, J. S.; Li, L. X.; Levkin, P. A. Porous Poly(2-Octyl Cyanoacrylate): A Facile One-Step Preparation of Superhydrophobic Coatings on Different Substrates. *J. Mater. Chem. A* **2013**, *1*, 1026−1029.
(27) Erbil, H. Y.; Demirel, A. L.; Avci, Y.; Mert, O. Transformation of a Simple Plastic into a Superhydrophobic Surface. *Science* **2003**, *299*, 1377−1380.
(28) Zhao, N.; Xie, Q.; Weng, L.; Wang, S.; Zhang, X.; Xu, J. Superhydrophobic Surface from Vapor-Induced Phase Separation of Copolymer Micellar Solution. *Macromolecules* **2005**, *38*, 8996−8999.
(29) Xie, Q.; Xu, J.; Feng, L.; Jiang, L.; Tang, W.; Luo, X.; Han, C. C. Facile Creation of a Super-Amphiphobic Coating Surface with Bionic Microstructure. *Adv. Mater.* **2004**, *16*, 302−305.
(30) Kato, S.; Sato, A. Micro/Nanotextured Polymer Coatings Fabricated by UV Curing-Induced Phase Separation: Creation of Superhydrophobic Surfaces. *J. Mater. Chem.* **2012**, *22*, 8613−8621.
(31) Nakajima, A.; Fujishima, A.; Hashimoto, K.; Watanabe, T. Preparation of Transparent Superhydrophobic Boehmite and Silica Films by Sublimation of Aluminum Acetylacetonate. *Adv. Mater.* **1999**, *11*, 1365−1368.
(32) Levkin, P. A.; Svec, F.; Frechet, J. M. Porous Polymer Coatings: A Versatile Approach to Superhydrophobic Surfaces. *Adv. Funct. Mater.* **2009**, *19*, 1993−1998.
(33) Wu, J.; Li, Y.; Chen, L.; Zhang, Z.; Wang, D.; Xu, C. Simple Fabrication of Micro/Nano-Porous SiOC Foam from Polysiloxane. *J. Mater. Chem.* **2012**, *22*, 6542−6545.
(34) Inoue, T. Reaction-Induced Phase Decomposition in Polymer Blends. *Prog. Polym. Sci.* **1995**, *20*, 119−153.
(35) Meng, F.; Zheng, S.; Li, H.; Liang, Q.; Liu, T. Formation of Ordered Nanostructures in Epoxy Thermosets: A Mechanism of Reaction-Induced Microphase Separation. *Macromolecules* **2006**, *39*, 5072−5080.
(36) Lipatov, Y. S.; Kosyanchuk, L. F.; Nesterov, A. F. Phase Separation in Blends of Linear Polymers Formed in Situ According to Different Mechanisms. *Polym. Int.* **2002**, *51*, 772−780.
(37) Park, J. W.; Kim, S. C. Phase Separation During Synthesis of Polyetherimide/Epoxy Semi-IPNs. *Polym. Adv. Technol.* **1996**, *7*, 209−220.
(38) Girard-Reydet, E.; Sautereau, H.; Pascault, J. P.; Keates, P.; Navard, P.; Thollet, G.; Vigier, G. Reaction-Induced Phase Separation Mechanisms in Modified Thermosets. *Polymer* **1998**, *39*, 2269−2279.
(39) Karstedt, B. D.; Scotia, N. Y. Platinum-Vinylsiloxanes. U.S. Patent 3,715,334, February 6, 1973.
(40) Gualandris, V.; Hourlier-Bahloul, D.; Babonneau, F. Structural Investigation of the First Stages of Pyrolysis of Si−C−O Preceramic Polymers Containing Si−H Bonds. *J. Sol−Gel Sci. Technol.* **1999**, *14*, 39−48.
(41) Belot, V.; Corriu, R. J. P.; Leclercq, D.; Mutin, P. H.; Vioux, A. Redistribution Reactions in Silsesquioxane Gels. *J. Mater. Sci. Lett.* **1990**, *9*, 1052−1054.
(42) Radovanovic, E.; Gozzi, M. F.; Gonçalves, M. C.; Yoshida, I. V. P. Silicon Oxycarbide Glasses from Silicone Networks. *J. Non-Cryst. Solids* **1999**, *248*, 37−48.
(43) Schiavon, M. A.; Radovanovic, E.; Yoshida, I. V. P. Microstructural Characterisation of Monolithic Ceramic Matrix Composites from Polysiloxane and SiC Powder. *Powder Technol.* **2002**, *123*, 232−241.
(44) Johnson, R. E., Jr.; Dettre, R. H. Contact Angle Hysteresis I. Study of an Idealized Rough Surface. *Adv. Chem. Ser.* **1964**, *43*, 112−135.
(45) Wenzel, R. N. Resistance of Solid Surfaces to Wetting by Water. *Ind. Eng. Chem.* **1936**, *28*, 988−994.
(46) Cassie, A. B. D.; Baxter, S. Wettability of Porous Surfaces. *Trans. Faraday Soc.* **1944**, *40*, 546−551.
(47) Lafuma, A.; Quere, D. Superhydrophobic States. *Nat. Mater.* **2003**, *2*, 457−460.
(48) McHale, G.; Shirtcliffe, N. J.; Newton, M. I. Contact-Angle Hysteresis on Super-Hydrophobic Surfaces. *Langmuir* **2004**, *20*, 10146−10149.
(49) Pilotek, S.; Schmidt, H. K. Wettability of Microstructured Hydrophobic Sol−Gel Coatings. *J. Sol−Gel Sci. Technol.* **2003**, *26*, 789−792.
(50) Li, W.; Amirfazli, A. Microtextured Superhydrophobic Surfaces: A Thermodynamic Analysis. *Adv. Colloid Interface Sci.* **2007**, *132*, 51−68.
(51) Boinovich, L.; Emelyanenko, A. M.; Pashinin, A. S. Analysis of Long-Term Durability of Superhydrophobic Properties under Continuous Contact with Water. *ACS Appl. Mater. Interfaces* **2010**, *2*, 1754−1758.
(52) Chang, K.-C.; Chen, Y.-K.; Chen, H. Fabrication of Highly Transparent and Superhydrophobic Silica-Based Surface by TEOS/PPG Hybrid with Adjustment of the pH Value. *Surf. Coat. Technol.* **2008**, *202*, 3822−3831.

NOTE ADDED IN PROOF

After this Article was accepted, the authors were made aware of another relevant article by Chen et al.[52] describing fabrication of highly transparent and superhydrophobic silica-based surfaces using a sol−gel process.